Numerical and Experimental Investigation on the Self-Healing Potential of Interpenetrating Metal–Ceramic Composites

Dominik Horny,* Joél Schukraft, Carolin Pieper, Kay André Weidenmann, and Katrin Schulz

An interpenetrating metal ceramic composite (IMCC) has been investigated regarding the potential as well as the feasibility of self-healing. Triggered by heating, cracks in the damaged composite located mainly in the Al_2O_3 ceramic or at the interface could be filled and closed by the liquid AlSi10Mg metal alloy. This healing procedure promises to reduce stress concentrations at crack tips and to improve the mechanical properties compared to the predamaged composite. Two different numerical approaches have been introduced to investigate this assumption and the potential of self-healed IMCCs for a best case scenario: 1) A simple 2D model to analyze the reduction of stress concentrations in front of a crack tip within the ceramic due to healing and 2) a 3D model based on CT-scan reconstructed microstructures to study how macroscopic mechanical properties can be restored depending on the amount of predamage. Further, the self-healing approach has been investigated experimentally for the same composite. Despite the fact that experimental self-healing of the investigated IMCC is only moderately feasible so far, the study shows the great potential that can still be exploited in order to extend the service life time of IMCC engineering components.

1. Introduction

With regard to the advancing climate change, a high level of sustainability is a major component of successful engineering today. Therefore, highly durable light-weight materials for structural applications play a key role in reducing greenhouse gases, especially in the mobility sector.[1] For safety relevant components, damage tolerance is another important feature which is provided, e.g., by light-weight metals. It has been shown that reinforcing these metals with ceramics can be used to tailor the mechanical and thermal properties. The resulting metal matrix composite (MMC) can outperform the pure metal regarding, e.g., strength, stiffness, hardness, and wear resistance, to enhance the reliability and the life cycle of the components.[2] Besides the raw material combination, also the reinforcement morphology has a major impact on the properties of an MMC.[3] Composites with an advanced, interpenetrating (also bi- or co-continuous) microstructure allows for an enhancement of various properties such as stiffness,[4,5] strength,[6] toughness,[7] wear,[8,9] as well as thermal expansion.[4,10] In particular, the possibility to combine and optimize two or more different features simultaneously, e.g., mechanical strength and thermal expansion or thermal/electrical conductivity,[11,12] thus creating multifunctional materials makes interpenetrating composites stand out compared to classical particle or fiber-reinforced MMCs.

Under a sufficiently high load (mechanical, thermal, etc.), even advanced high-performance materials will eventually undergo damage. Besides a good recyclability, restoring the functionality of damaged components and extending their service life time become increasingly relevant for sustainable engineering applications. Inspired by the ability of natural materials, like human bones or skin, to recover from physical damage by biological healing processes,[13] first concepts for engineering materials with self-healing capabilities were introduced over 20 years ago using hollow fibers[14] or capsules[15] containing a healing agent. They are based on encapsulated reactive fluids that are released upon crack intrusion and polymerize in the cracked areas (triggered by embedded catalysts). Besides these pioneering

D. Horny, K. Schulz
Institute for Applied Materials - Reliability and Microstructure (IAM-ZM)
Karlsruhe Institute of Technology (KIT)
76131 Karlsruhe, Germany
E-mail: dominik.horny@kit.edu

D. Horny, K. Schulz
Institute of Applied Research (IAF)
Hochschule Karlsruhe - University of Applied Sciences (HKA)
76012 Karlsruhe, Germany

J. Schukraft, C. Pieper, K. A. Weidenmann
Institute of Materials Resource Management (MRM)
University of Augsburg
86159 Augsburg, Germany

ⓘD The ORCID identification number(s) for the author(s) of this article can be found under https://doi.org/10.1002/adem.202300259.

**ADVANCED
SCIENCE NEWS**

www.advancedsciencenews.com

**ADVANCED
ENGINEERING
MATERIALS**

www.aem-journal.com

concepts, other techniques have been developed, using reversible cross-links,[16] interdiffusion (already investigated in the 1980s),[17] shape memory components,[18] electrical conductivity, multiphase morphologies,[19] nanoparticle migration,[20] and co-deposition[21] to accomplish healing. For an overview of the numerous approaches, we refer to the following review papers.[13,22–24]

As most of the presented healing concepts are well compatible with the energetic properties of polymers, the research on self-healing materials is dominated by polymer systems.[25] However, from a mechanical perspective, self-healing polymers inevitably lack sufficient mechanical strength to be used as structural materials in many engineering components.[26,27] In this regard, research on the self-healing of metals and MMCs has been of interest in the past years. Similar to polymer materials, concepts like encapsulation of a metallic solder, shape-memory alloys, or electro-(chemical) healing can be used in metals as well.[28] However, a much higher external energy trigger is necessary, e.g., to break metallic bonds and transport the healing agent to the cracks.[26] According to Gosh et al.,[29] self-healing in metals can therefore be mainly classified as nonautonomous as an external intervention, i.e., by means of heat, is necessary. Materials that can heal damages without external triggers are defined as autonomic self-healing materials (so far exclusively polymers). The most studied concept for metals is precipitation healing, which is based on supersaturated metal alloys. Voids formed during the damage phase are preferred nucleation locations for precipitates of the solute atoms which close these voids.[25] However, this works only for very small voids on the nanometer length scale. A more promising approach is the introduction of ceramic capsules or tubes containing a low-melting metal into the metallic matrix. In case of damage, the ceramic shell is broken, and the contained metal flows into the crack upon heating to its melting temperature.[30,31]

Although the investigation on self-healing strategies for metals has been increased in the past decade, it is still in its infancy,[25] and there is even less knowledge in the field of metal–ceramic composites. In all previous studies in this field, the materials have been specifically designed to have a self-healing capability. On the contrary, this does not apply to the Al_2O_3/AlSi10Mg lightweight composite investigated in this study. However, the big difference in melting temperatures between the metal and in the ceramic and the fact that cracks in MMCs initiate in the high melting ceramic phase offer a self-healing potential for these materials the material class. This applies in particular to interpenetrating metal ceramic composites, as the interconnected ceramic serves as a backbone for mechanical stability even if the metal is re-molten. Therefore, the authors think that healing of the composite might be a special, additional feature of the material due to its interpenetrating microstructure which can be seen as a lot of connected, low-melting tubes or a vascular network of Al-alloy within a ceramic.

This study serves as a first approach to investigate the (self-)healing potential of interpenetrating metal–ceramic composites numerically using idealized assumptions to reveal the upper limit for the restoration of mechanical properties. It underlines the great opportunities that healing approaches potentially offer to extend the lifetime of predamaged IMMC

engineering components and motivate further research in this field. In addition, first attempts at experimental feasibility are presented, and possible key points for future investigations are discussed.

2. Materials and Approaches

2.1. Composite Material

The investigated material is a macroscopically homogeneous, interpenetrating metal ceramic composite (IMCC) containing an Al_2O_3 ceramic and an AlSi10Mg metallic phase. It is manufactured by gas pressure infiltration of the molten aluminum alloy into a highly porous open-cell alumina foam. The porous ceramic preform with a relative density of approx. 26% is provided by Morgan Advanced Materials Haldenwanger GmbH.[32] A detailed description of the infiltration process and a characterization of the microstructure are provided elsewhere.[33,34] For the numerical simulations, the material microstructure has been reconstructed, filtered, and mashed based on X-ray CT-scans as described in ref. [35].

2.2. Self-Healing Concept

As recent studies on the interpenetrating Al_2O_3/AlSi10Mg composite have shown, first cracks mainly occur in the ceramic or at the interface when loaded under compression.[34,35] The idea is to heal these cracks by using the AlSi10Mg as the low-melting filler. Therefore, heat is applied as a trigger to melt the close eutectic aluminum alloy ($T_m \approx 550\,°C$), whereas the ceramic foam remains unaffected by this temperature. If all of the cracks in the ceramic could be healed in this procedure, this would ideally result in a material that is comparable to the pristine composite.

However, the physical properties of the investigated material system have to be considered in order to develop a successful healing approach. The combination of aluminum oxide and aluminum alloy is well known for poor wetting,[36] i.e., negative capillary pressure. Hence, gas pressure is necessary to force the aluminum melt into the porous ceramic foam during material manufacturing. Therefore, it can be concluded that penetration of cracks by the molten alloy is only possible with external gas pressure support. The experimental investigations aim to analyze the influence of the these challenges on the (self-)healing success.

Complementary to this, the numerical investigations aim to investigate the differences in the mechanical behavior of pristine, damaged and healed composites under the assumption of optimal healing success. The focus is to determine the extent to which healing can reduce stress concentrations in front of cracks and restore mechanical properties of the composite at best.

2.3. Healing Efficiency

In order to measure the (self-) healing success, a quantitative description is necessary. In the literature, various definitions for the so-called healing efficiency η exist. The most common

proposal (see e.g.)[37–39] is to use the ratio of the healed (h) and the pristine (p) material property

$$\eta_1(f) = \frac{f^{\mathrm{h}}}{f^{\mathrm{p}}} \tag{1}$$

where f is the property of interest. Another definition to quantify healing according to Blaizik et al.[22] uses the ratio of material property changes

$$\eta_2(f) = \frac{f^{\mathrm{h}} - f^{\mathrm{d}}}{f^{\mathrm{p}} - f^{\mathrm{d}}} \tag{2}$$

where the superscript d denotes the damaged material.

3. Modeling

Two different numerical models are used to investigate the self-healing potential of the IMCC: A simplified 2D model to analyze how stress concentrations in front of a crack tip within a ceramic rod of the composite can be reduced and a 3D microstructure model to investigate the restorability of mechanical properties depending on the amount of predamage.

3.1. 2D Crack Tip Model

As mentioned in Section 2.1, investigation on the damage behavior has shown that cracks start to initiate at the boundary of the ceramic rods close to the interface at the top and the bottom of the AlSi10Mg filled cavities. Considering such cracks as a boundary notch in a ceramic cuboid (or plate in 2D), the stress field resulting from external loading can be described by means of linear elastic fracture mechanics (LEFM) using the stress intensity factors (SIFs) introduced by Irwin.[40,41]

(Self-)healing aims to prevent crack growth upon loading and extend the materials lifetime by closing cracks, thus reducing the SIF in front of sharp crack tips. However, most numerical (self-)healing studies focus either on stress concentrations during the initial damage (prior to healing),[15,42] the healing process itself,[31,43–47] or on the material properties after healing.[44–49] Only a few studies by Xue and coworkers[50,51] investigate local stress distributions in healed concrete structures.

In ref. [50], the interface crack initiation and propagation behavior of concrete healed with different healing agents are studied in three-point bending simulations. In ref. [51], the bonding behavior of the interface between healing agent and concrete crack has been investigated by analyzing the local stress distributions at the interface.

However, the question remains to what extend stress concentrations at notch tips are reduced by the healing. The 2D model presented in the following aims to answer this question for cracks in Al₂O₃ healed with an AlSi10Mg alloy.

To investigate the stress concentration in the ceramic caused by an initial crack, a simplified 2D geometry with a V-shaped notch of length a and opening angle α has been modeled within a ceramic rod of width w and height $2h$ with $h = w$ as depicted in **Figure 1** on the left. Using symmetry boundary conditions at the center
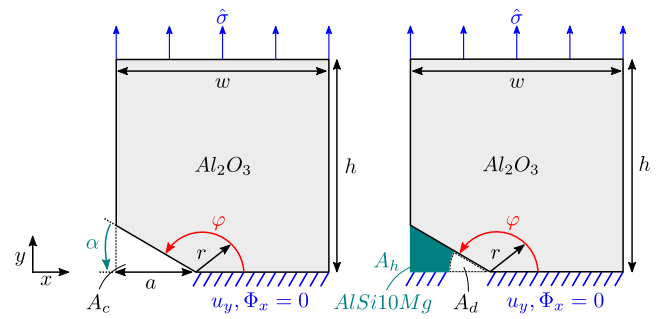
Figure 1. Schemes of the notch model with a crack (left) and a healed crack (right) in the Al₂O₃ ceramic used to investigate the stress concentration infront of the crack tip.

$$u_y, \Phi_x = 0, \quad \text{at } y = 0 \tag{3}$$

with a fixed displacement in y-direction u_y and no rotation around the x-axis Φ_x only the upper half of the rod has been used in the numerical calculations. A tensile load in y-direction perpendicular to the crack $\hat{\sigma} = 100\,\mathrm{MPa}$ representing the most critical loading condition for crack propagation (mode I) is applied at the top. The mechanical stresses are subsequently evaluated at a distance r in front of the crack tip depending on the angle φ.

The potential reduction of stresses in front of the tip due to healing is investigated by replacing a certain amount of the initial crack area A_c with AlSi10Mg as shown in Figure 1 on the right. It is assumed that the crack is healed by the metal alloy from the remote side of the tip showing a concave front. The healed area A_h and the remaining damage cavity A_d at the crack tip add up to the initial crack volume $A_c = A_h + A_d$. The metal–ceramic interface is assumed to be perfectly tied. By varying the amount of crack healing $A_h/A_c \in \{0.5, 0.6, 0.7, 0.8, 0.9, 1.0\}$, the crack length ratio $a/w \in \{0.2, 0.3, 0.4, 0.5, 0.6\}$, and the crack opening angle $\alpha \in \{7.5°, 15°, 22.5°, 30°, 37.5°, 45°\}$, it is studied how healing affects the stresses in the ceramic depending on the healing success, the predamage levels, and different crack shapes.

Linear, elastic, isotropic behavior is considered for the Al₂O₃, whereas the AlSi10Mg is modeled using an elasto-plastic behavior assuming J_2 plasticity, isotropic hardening with the yield function

$$f(\sigma, k) = \overline{\sigma} - k = 0 \tag{4}$$

including the equivalent stress $\overline{\sigma} = \sqrt{3J_2}$, the second invariant of the stress tensor J_2 and the yield stress k.

A rate independent Swift hardening law[52] is used to describe the evolution of k with respect to the equivalent plastic strain $\overline{\varepsilon}_{\mathrm{pl}}$ reading

$$k(\overline{\varepsilon}_{\mathrm{pl}}) = A(\overline{\varepsilon}_{\mathrm{pl}} - \varepsilon_0)^n \tag{5}$$

with the hardening parameters $\{A, \varepsilon_0, n\}$. All relevant material parameters are listed in **Table 1**.

**ADVANCED
SCIENCE NEWS**

www.advancedsciencenews.com

**ADVANCED
ENGINEERING
MATERIALS**

www.aem-journal.com

Table 1. Material input parameter. Tensile strength σ_t^I and yield strength σ_y are uniquely defined for the Al$_2$O$_3$ and the AlSi10Mg, respectively. Yield strength σ_y corresponds to yield stress at zero plastic strain $k(\overline{\varepsilon}_{pl} = 0)$.

Parameter		Unit	Al$_2$O$_3$	AlSi10Mg
Young's modulus	E	GPa	350	70
Poisson ratio	ν	–	0.23	0.32
Tensile/yield strength	σ_t^I/σ_y	MPa	450	201.22
Fracture energy	G_f^I	J m^{-2}	50	–
Hardening parameter	A	MPa	–	442.67
	ε_0	–	–	0.001
	n	–	–	0.112

3.2. 3D Microstructure Model

Reconstructions from X-ray CT-sans of the microstructure are the basis for the geometrical representation of the 3D numerical model. Within the scanned samples, a region of interest (ROI) with an edge length of approx. 2 mm has been chosen and the ROI images have been binarized, segmented and filtered according to ref. [33]. A cubic cutout of the ROI with an edge length of 133 μm and a ceramic volume fraction of 26% have been randomly chosen, smoothed, and meshed as described in ref. [35].

Regarding the constitutive behavior, the aluminum alloy is modeled as described in Section 3.1 (see Equation (4) and (5)). For the ceramic, a Rankine damage initiation criterion depending on the tensile strength σ_t^I and a regularized continuum damage model with multidirectional smeared cracking assumption describing the linear softening depending on the fracture energy G_f^I is introduced in addition to the isotropic, linear elastic behavior up to σ_t^I. The general relation between G_f^I, σ_t^I and the crack opening displacement u reads

$$G_f^I = \int \sigma_t^I du \qquad (6)$$

If u reaches u_0 with $u_0 = 2G_f^I(\sigma_t^I)^{-1}$, i.e., the stiffness reaches zero, the respective element is considered to be completely failed and is excluded from the calculation in order to avoid nonphysical distortions.

A compressive load with a strain rate of $\dot{\varepsilon}_y = 10^{-1}$ is applied on the cubic composite volume using two rigid plates both on top (moving) and on the bottom (fixed), see also.[34,35] No friction is assumed between the plates and the material and the interface between ceramic and aluminum is considered to be perfectly tied. The investigated microstructure and the boundary conditions are shown in **Figure 2**. As a first step, the pristine (undamaged) composite is compressed up to a total stain of 3% and steadily undergoes increasing damage. At five different damage stages, all finite elements that failed are considered to be cracks which can potentially be healed. In a numerical healing routine, the failed ceramic elements are replaced by AlSi10Mg as depicted schematically in **Figure 3**. Like the pristine IMCC, the damaged and the healed microstructures are (re-)loaded up to a total stain of 3%. From the results, healing efficiencies according to Equation (1) and (2) are derived for different mechanical characteristics.
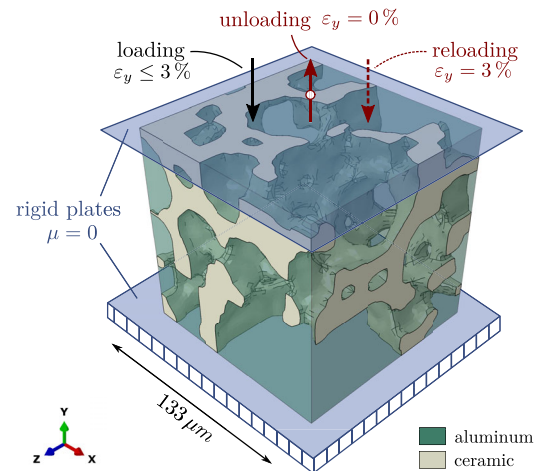
Figure 2. Boundary conditions for the 3D microstructure compression model.
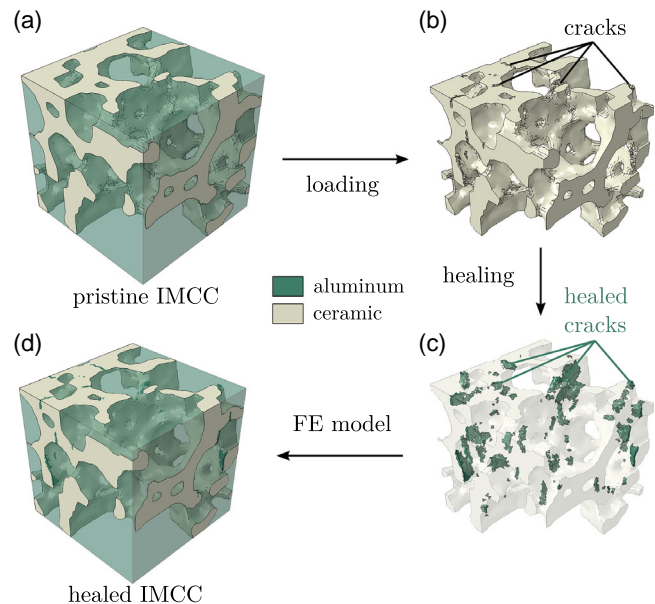
Figure 3. Schematic visualization of the numerical healing procedure. a) First, the pristine interpenetrating Al$_2$O$_3$/AlSi10Mg composite is loaded up to a certain strain. b) The ceramic phase undergoes damage and completely failed elements are considered to be cracks that can potentially be healed by metal infiltration. c) In a numerical routine, the cracks are identified and healed by inserting the AlSi10Mg phase. d) The healed ceramic phase is combined with the original metal phase to create a FE-model of the healed IMCC.

4. Experimental Section

In order to test self-healing feasibility of the material experimentally, damage had to be introduced to the samples first. Then, the samples had been subjected to different healing attempts. The microstructure of the specimens had been examined by computed tomography in the damaged state and after the healing experiments, in order to evaluate the effectiveness of the (self-)

healing approaches. Within the Avizo software framework, an algorithm has been developed to enable the 3D visualization and quantification of crack volumes in the interpenetrating composite. Finally, the elastic stiffness in compression direction had been measured using ultrasound phase spectroscopy to determine the healing efficiency with respect to the mechanical properties.

4.1. Sample Preparation

Specimens were extracted from the infiltrated material with a diamond wire saw DWS 250 by Diamond WireTec GmbH & Co. KG and a hollow diamond drill. The cylindrical specimens used for the self-healing approach, and the soldering attempt had a mean diameter of 3.8 mm; a height of approx. 8 mm and parallel polished end faces according to DIN 50134.[53] For the alloy-supported healing approach, a parallelepiped measuring $30 \times 23 \times 5\ mm^2$ has been cut, surface grinded and then drilled into the surface extension using a hollow diamond drill with a diameter of 18 mm. Images of the sample geometries are shown in **Figure 4**.

4.2. Predamaging

The samples were systematically predamaged compression tests in the universal testing machine ZwickRoell Z1464 with a nominal strain rate of $0.06\ 1\ s^{-1}$. Different extents of damage were introduced, similar to the modelled load stages in Section 3.2. Based on previous experiments on the damage behavior of the material system,[34,54] four different damage states have been selected in order to introduce cracks with varying thickness. For the first damage state, the test was aborted after reaching a stress of 350 MPa, which is generally below the materials' average compressive strength of 400 MPa. Higher levels of damage were induced by stopping the test after reaching the compressive strength at force drops of 1%, 5%, and 7% with respect to the maximum force. Due to the experimental course of the healing approaches, the damage state had no significant influence on the results and was therefore not considered further.

4.3. (Self-)Healing Experiments

Various healing procedures were tested and investigated on the predamaged specimens. The definition of the term self-healing[29] includes the application of different kinds of external triggers but excludes the addition of alloy to achieve healing. Because of that the performed experiments can be further divided into self-healing and healing treatments, the latter involving the addition of alloy. Besides that, soldering of cracks has been investigated (cf. **Table 2**). Some of the cylindrical samples have been coated with boron nitride and/or embedded in plaster prior to the (self-)healing approach. The top surface of the specimen was left uncovered from plaster as shown in Figure 4.

4.3.1. Preliminary Test and Self-Healing Approach

In the preliminary test (cf. Table 2, P-A-1-650), only thermal energy was used as healing activator. A predamaged cylindrical sample was heated at $10\ K\ min^{-1}$ to a maximum temperature of 650 °C in a conventional furnace by Nabertherm. After a holding time of 5 min, the sample was cooled to room temperature.

Temperature and pressure-assisted self-healing was carried out in the gas pressure infiltration device described by the authors in Horny et al.[33] The original setup was altered for the purpose of sample healing (see **Figure 5**).

The sample was placed in a crucible together with calcined kaolin powder as support material. For an accurate temperature control, the thermocouple was positioned as close as possible to the sample. Similar to the manufacturing of the composite, a vacuum of 0.06 mbar was used during heating with a heating rate of $10\ K\ min^{-1}$. At a temperature of 550 °C, just before reaching the solidus temperature of the alloy, a prepressure was applied. Then, heating was continued up to a certain maximum temperature above the liquidus temperature of the alloy and additional gas pressure up to 60 bar was applied. Finally, cooling was performed while maintaining the maximum pressure. For the self-healing experiments performed in vacuum, no pressure was applied, and the vacuum was maintained for the whole process. The atmosphere, temperature, and pressure were varied in different experiments for plaster-embedded and raw samples. Detailed experimental conditions are given in Table 2.

#### 4.3.2. Alloy-Supported Healing Approach

A sufficient amount of AlSi10Mg alloy was placed on the top surface of the parallelepiped prior to temperature and pressure-assisted healing in the gas pressure infiltration setup. The aluminum-supported healing experiments were carried out similar to the description in Section 4.3.1, but without any prepressure.
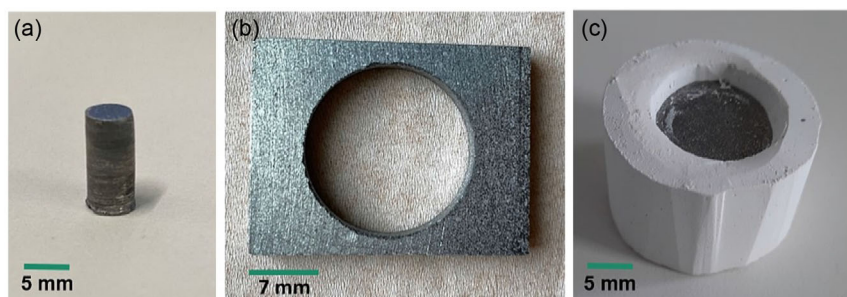
Figure 4. Pictures of a) cylindrical samples and b) parallelepiped samples used for the (self-)healing approaches. A plaster-embedded cylindrical sample is shown in c).

Table 2. Overview of the tested samples and parameter variation for healing and self-healing approaches.

Experimental approach	Sample name	Sample geometry	BN-Coating	Plaster-embedding	Additional alloy	Atmosphere	Prepressure [bar]	Max. pressure [bar]	Max. temp. [°C]
Preliminary test	P-A-1-650	Cylinder	✗	✗	✗	Air	–	–	650
Self-healing approach	SH-Ar-P5_60-650	Cylinder	✗	✗	✗	Argon	Five	60	650
	SH-Vac-0-630	Cylinder	✗	✗	✗	Vacuum	–	–	630
	SH-N-P5_60-630	Cylinder	✗	✗	✗	Nitrogen	Five	60	630
	SH-Ar-P5_60-630	Cylinder	✓	✗	✗	Argon	Five	60	630
	SH-Ar-P10_60-700	Cylinder	✓	✓	✗	Argon	10	60	700
	SH-Ar-P15_60-700	Cylinder	✓	✓	✗	Argon	15	60	700
Healing approach	H-Ar-60-700	Parallel-epiped	✗	✗	✓	Argon	–	60	700
Soldering of the cracks	SC-A-1-500	Cylinder	✗	✗	✓	Air	–	–	500
	Sample one	Cylinder	✗	✗	✓	Air	–	–	500
	Sample two	Cylinder	✗	✗	✓	Air	–	–	500
	Sample three	Cylinder	✗	✗	✓	Air	–	–	500
	Sample four	Cylinder	✗	✗	✓	Air	–	–	500
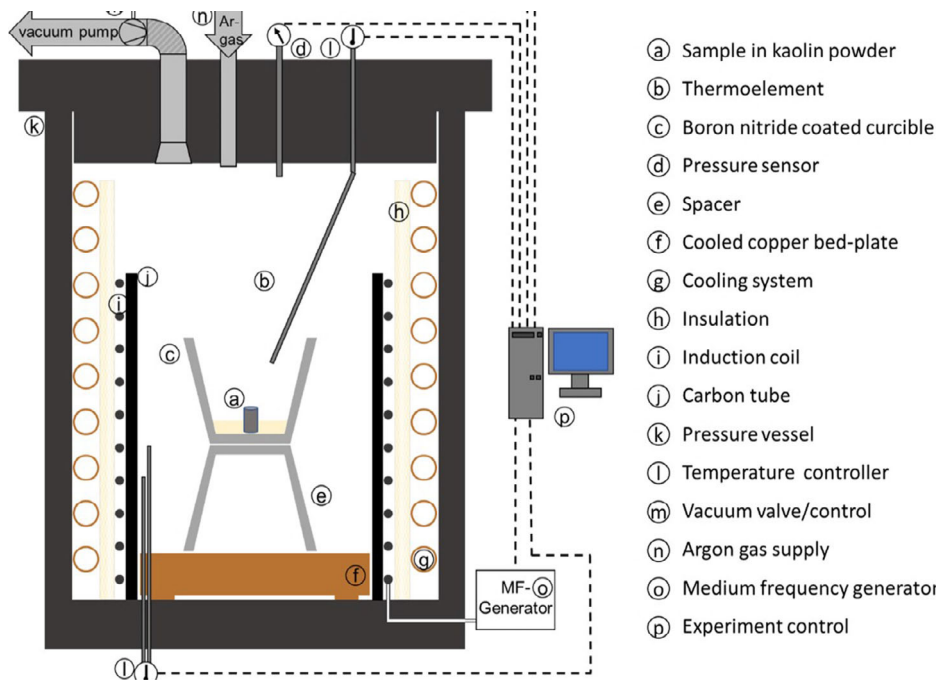
Figure 5. Gas pressure infiltration setup for pressure-assisted (self-)healing experiments according to ref. [64].

4.3.3. Crack Soldering

A soldering attempt was carried out to investigate the influence of the alloy passivating layer on the healing success. For this purpose, a capillary-driven S-ZnAl22 solder wire (AF 665 NH by Fontargen) filled with noncorrosive flux was used as healing agent. After heating both the sample and the wire to the solders' melting temperature (420–480 °C), the entire surface of the pre-damaged sample was covered with the solder melt until crack filling could be observed.

4.4. Microstructural Characterization and Evaluation

An X-ray computer tomography system (Phoenix Nanotom M) by General Electrics equipped with a diamond target was used for microstructural characterization. The software components Phoenix data sx2 acquisition and Phoenix data sx2 reconstruction, both by GE Sensing & Inspection Technologies GmbH, were applied to process the data and reconstruct a 3D image of the sample. The beam source was operated at 80 kV and 180 μA, and the integration time was set to 2000 ms, averaging three images for

each of the 1000 positions per 360°. A detector sensitivity of two was selected to increase the contrast between the sample and the background. With a focus-object distance (FOD) of 10.5 mm and a focus-detector distance (FDD) of 300 mm for cylindrical shaped specimens, the resulting CT data had a voxel size of 3.5 µm^3. Other scanning parameters had to be used for sample H-Ar-60-700 due to the different dimensions: An FOD of 24 mm and an FDD of 480 mm were chosen, yielding a voxel size of 5 µm^3.

Each specimen was scanned three times: In the undamaged state, immediately after predamage, and after the healing attempt. For the CT-scans of the solder-healed samples, a tin sheet of 0, 3 mm thickness was placed behind the aperture to decrease the beam hardening resulting from the tin consisting solder.

Evaluation of the CT data was carried out with the Avizo software by ThermoFisher scientific. The aim was to compare the CT data of a sample in predamaged and healed state considering changes in crack volume. This was achieved by the following two major procedures, with the Avizo-specific operations displayed in italic letters.

The first procedure was required to align the 3D-data in the coordinate system of the software and therefore ensure comparability of both data sets. By applying *Register Images*, one of the data sets was visually realigned with the second data set serving as a reference. The module *Resample Transformed Image* generates a new data set corresponding to this alignment. By using *Extract Subvolume*, the Bounding Box of the reference data set was adapted to the one of the realigned data. The result of this procedure is an identical position of both sample volumes enabling a qualitative comparison of the sample microstructure.

For the quantitative analysis of the crack volume before and after healing, further processing of the aligned datasets was necessary. Step 1 was an Image Stack Processing workflow including an *AutoThresholding* module as well as subsequent operations to extract the darker grey values, which are representative for the cracks but also for the pores and artifacts. Step 2 was applied on the CT data of the predamaged sample only. In order to remove artifacts and pores from the resulting data, first labeling and then filter by measure range using the shape function *ShapeVA3d* were applied. The value one of this function corresponds to a perfect sphere, whereas higher values represent less compact objects. By setting the minimum threshold of the function *ShapeVA3d* to a value of 50, most spherical objects, i.e., pores and artifacts, were removed from the 3D-data, with only the crack volume of the predamaged sample remaining.

In step 3, the crack volume of the healed sample was obtained. Using the tool *Arithmetic*, the overlap of the data set representing the crack volume of the predamaged sample and the data of the healed sample resulting from step 1 was calculated. By this, only the objects of the healed samples data set, that are in the same area as the crack volume are displayed. This ensured that porosity and debonding in the crack area could be considered in the quantitative comparisons. Step 4 included the crack volume calculation for both data sets by using *VolumeFraction*. The entire crack segmentation process is shown schematically in **Figure 6**.

4.5. Ultrasonic Phase Spectroscopy

In order to investigate the influence of the healing procedure on the mechanical properties, the elastic stiffness in compression
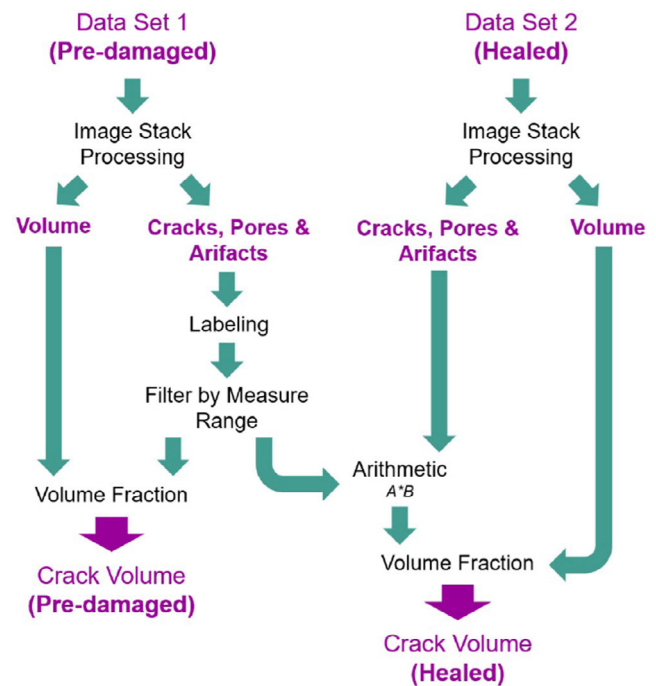
Figure 6. Illustration of the algorithm developed in the Software Avizo to obtain quantitative crack volumes from CT-data of predamaged and healed specimens. Input and output data are colored in purple letters, and module names are colored black.
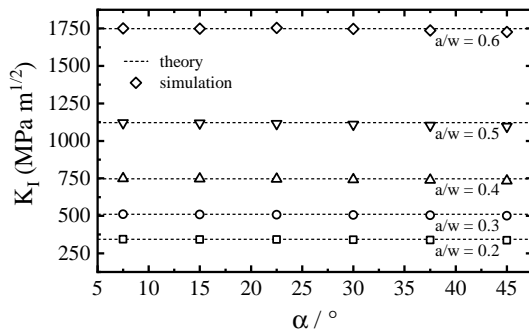
direction has been measured via ultrasonic phase spectroscopy (UPS). Elastic behavior is determined in the pristine (c.f. Section 4.1), damaged (c.f. Section 4.2), and healed (c.f. Section 4.3.3) state of the IMCC to evaluate the healing efficiency (see Equation (1) and (2)). The measurements are performed using an electronic network analyzer type R3754A by Advantest (Tokyo, Japan). A dektop computer with the LabView evaluation software by National Instrument (Austin, USA) computer and longitudinal ultrasonic contact transducers V122-RM, by Olympus Deutschland GmbH, (Hamburg, Germany) were connected to the network analyzer.

For testing, the specimens were clamped between the transmitting and receiving transducers, covered with a bubble-free, thin layer of a coupling medium (treacle) and measured three times in a frequency range of 10 kHz–10 MHz. The resulting squared sound velocity was multiplied by the density of the respective sample (calculated from Archimedes principle measurements) and averaged between the three measurements to determine the elastic constant C_{22}. Further details on the method can be found in Horny et al.[33]

5. Results

5.1. 2D Crack Tip Model

To validate the model assumptions as well as the FEM-mesh used in the 2D crack tip model, mode I stress intensity factors K_I of the cracked ceramic ($A_h/A_c = 0$) for different a/w ratios and angles α have been determined and compared to theoretical

**ADVANCED
SCIENCE NEWS**

www.advancedsciencenews.com

**ADVANCED
ENGINEERING
MATERIALS**

www.aem-journal.com

Figure 7. Stress intensity factors (SIF) for the cracked ceramic for different a/w ratios depending on the crack opening angle α. Theoretical SIF values for according to ref. [55] displayed for comparison.

values according to Liu et al.[55] as shown in **Figure 7**. The K_I values have been calculated from the J-Integral according to ref. [56]. It is found that K_I values converge if more than eight node contours around the crack tip are evaluated. It is observed that the SIF is strongly dependent on the a/w ratio, as expected from theoretical expressions. As the numerical model contains a perfectly sharp V-notch, an infinitely high stress singularity is introduced at the crack tip independent of the opening angle α. Therefore, the dependence of K_I on the opening angle α is negligible. However, a small decrease of K_I is observed with increasing α for every a/w ratio.

As presented in Section 3.1, the healing effect on the damaged ceramic phase is investigated by the stress reduction of the most critical stress σ_y in front of the crack tip. It is found that the radial stresses very close to the crack tip (within the first element contour) exhibit nonphysical profiles. Therefore, a meaningful evaluation can only be made at a certain distance from the tip (cf. Figure 1). Here, a distance of r with $r/w = 0.015$ has been chosen and the stresses of the cracked σ_y^c and the healed σ_y^h ceramic are compared regarding different healing ratios A_h/A_c, crack length ratios a/w, and crack shapes α. It has to be noted that the stress ratios coincide with those evaluated at other distances r. The results are presented for selected parameter sets in **Figure 8** and 9.
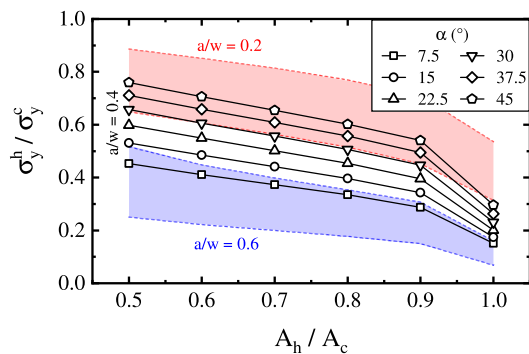
Figure 8. Ratio of stresses in y-direction (mode I) in the healed σ_y^h and cracked σ_y^c ceramic rod at $a/w = 0.4$ depending on the healing ratio A_h/A_c for different angles α. Stress ratio ranges for $a/w = 0.2$ (red) and $a/w = 0.6$ (blue) are displayed for comparison. All values have been extracted at $r = 0.15$ and $\varphi = 0$.
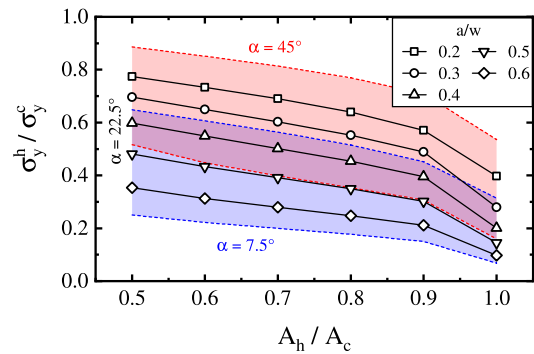
Figure 9. Ratio of stresses in y-direction (mode I) in the healed σ_y^h and cracked σ_y^c ceramic rod at $\alpha = 22.5°$ depending on the healing ratio A_h/A_c for different a/w ratios. Stress ratio ranges for $\alpha = 7.5°$ (red) and $\alpha = 45°$ (blue) are displayed for comparison. All values have been extracted at $r = 0.15$ and $\varphi = 0$.

Figure 8 shows the stress ratio σ_y^h/σ_y^c for a fixed crack length ratio $a/w = 0.4$ over the healing ratio A_h/A_c for different opening angles α. The simulation results are plotted using points with different marker shapes depending on α. The lines between the markers serve for visualization purposes only. As expected, σ_y^h/σ_y^c decreases with increasing A_h/A_c for all α. For healing ratios between 0.5 and 0.9 an almost constant decline in the stress ratio is observed. Between 0.9 and the fully healed crack at $A_h/A_c = 1.0$, the slope decreases significantly. For example, for an opening angle of 30° (downward triangle in Figure 8), the stress ratio reduces from 0.66 at $A_h/A_c = 0.5$ to 0.45 at $A_h/A_c = 0.9$. This results in a stress reduction range of $\Delta_{0.5-0.9}^{30°} = [\sigma_y^h/\sigma_y^c]_{0.5}^{30°} - [\sigma_y^h/\sigma_y^c]_{0.9}^{30°} = 0.21$. Considering $\sigma_y^h/\sigma_y^c = 0.23$ at a healing ratio of 1.0, almost the same stress reduction range $\Delta_{0.9-1.0}^{30°} = 0.22$ is covered between $A_h/A_c = 0.9$ and 1.0 only.

Another observation is that the stress reduction due to healing increases with decreasing opening angle α for all A_h/A_c ratios. Exemplary, the stress ratio at $A_h/A_c = 0.5$ is approx. 0.76 for $\alpha = 45°$ and decreases to 0.45 at $\alpha = 7.5°$. As for the healing ratio variation, a stress ratio range between $\alpha = 45°$ and $\alpha = 7.5°$ at a constant A_h/A_c can be defined. For $A_h/A_c = 0.5$, this range reads $\Delta_{0.5}^{\alpha} = [\sigma_y^h/\sigma_y^c]_{0.5}^{45°} - [\sigma_y^h/\sigma_y^c]_{0.5}^{7.5°} = 0.31$. At a healing ratio of 0.9, this range reduces to $\Delta_{0.9}^{\alpha} = 0.25$ with $[\sigma_y^h/\sigma_y^c]_{0.9}^{45°} = 0.54$ and $[\sigma_y^h/\sigma_y^c]_{0.9}^{7.5°} = 0.29$. The smallest range is observed at $A_h/A_c = 1.0$ where $[\sigma_y^h/\sigma_y^c]_{1.0}^{45°} = 0.30$, $[\sigma_y^h/\sigma_y^c]_{1.0}^{7.5°} = 0.15$ and $\Delta_{1.0}^{\alpha} = 0.15$.

For comparison, the σ_y^h/σ_y^c ranges between $\alpha = 7.5°$ and $\alpha = 45°$ for the maximum and minimum crack length ratios $a/w = 0.6$ and $a/w = 0.2$ are plotted in Figure 8 as blue and red areas, respectively. It can be noted that the stress ratio as well as the healing ratio range Δ^{α} decreases with increasing a/w ratio. Further, the range ratio between small and large A_h/A_c values $\Delta_{0.5}^{\alpha}/\Delta_{0.9}^{\alpha}$ increases with increasing crack length.

Analogously to Figure 8, the stress ratio σ_y^h/σ_y^c is plotted over A_h/A_c for a fixed angle $\alpha = 22.5°$ and varying a/w ratios in Figure 9. Again, the slope of the stress ratio decreases for all a/w ratios, most significantly for A_h/A_c ratios between 0.9 and 1.0. The crack length ratio has a significant impact on the

stress reduction as the stress ratio range at a constant A_h/A_c ratio $\Delta_{A_h/A_c}^{a/w} = [\sigma_y^h/\sigma_y^c]_{A_h/A_c}^{0.2} - [\sigma_y^h/\sigma_y^c]_{A_h/A_c}^{0.6}$ imposes. For the chosen angle $\alpha = 22.5°$, the ranges $\Delta_{0.5}^{a/w} = 0.42$ and $\Delta_{1.0}^{a/w} = 0.30$ are larger than the respective ranges due to an opening angle variation at constant a/w (cf. Figure 9). The ranges for minimum and maximum opening angles $\alpha = 7.5°$ and $\alpha = 45°$, depicted as blue and red areas in Figure 9, respectively, show that the influence of the a/w ratio decreases for smaller angles (compared to the respective range).

5.2. 3D Microstructure Model

As described in Section 3.2, the pristine IMCC is loaded up to a compressive strain of 3%. The mechanical stress–strain response is displayed in **Figure 10** as a black solid line. Values of the characteristic properties, i.e., elastic modulus E^p, compressive strength σ_{max}^p, and residual strength σ_{res}^p, of the pristine material (superscript p) are given in **Table 3**. Here, σ_{res} is defined as the strength at a compressive strain of $\varepsilon = 3.0\%$. During loading, the ceramic phase undergoes a successive damage process as
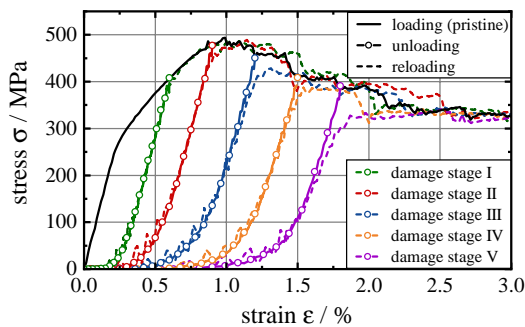
Figure 10. Stress–strain curves of the pristine composite under compressive loading (black solid line), unloading at different load/damage stages I–V (colored lines with circle symbols) and reloading behavior of the damaged composite (colored dashed lines).

Table 3. Elastic modulus E, compressive strength σ_{max}, and residual strength σ_{res} (at a strain of $\varepsilon = 3.0\%$) of the pristine and the healed microstructure at different healing stages I–V (analogous to damage stages) and corresponding healing efficiency coefficients η_i for each parameter.

Parameter	Healing Stage					
	Pristine	I	II	III	IV	V
E [GPa]	119.9	119.8	118.9	114.7	110.2	107.1
σ_{max} [MPa]	493.8	492.9	492.0	480.5	466.3	443.2
σ_{res} [MPa]	326.2	331.3	343.4	355.1	379.8	384.5
η_1 (E)	–	0.999	0.992	0.957	0.919	0.893
η_1 (σ_{max})	–	0.998	0.996	0.973	0.944	0.898
η_1 (σ_{res})	–	1.016	1.053	1.089	1.164	1.179
η_2 (E)	–	0.966	0.851	0.634	0.529	0.543
η_2 (σ_{max})	–	0.880	0.891	0.799	0.742	0.670
η_2 (σ_{res})	–	−1.68	−4.38	−8.03	54.60	26.35

described in the authors' previous works.[34,35] The fraction of damaged ceramic elements (i.e., elements in which the Rankine damage initiation criterion is met) and the failed ceramic elements (i.e., elements that are fully damaged according to Equation (6) and lost their load carrying capability) plotted over the loading strain of the pristine IMCC are shown in **Figure 11**.

For the investigation of the healing efficiency in dependence of a varying predamage, five damage stages marked I–V and highlighted with colored circles in Figure 11 are picked. Damage stage I at a total strain of $\varepsilon = 0.6\%$ and a failed ceramic fraction of $v_f = 0.001$ are located before the compressive strength of the pristine material at $\varepsilon = 0.99\%$ (cf. Figure 11 and 10). Stage II with $\varepsilon = 0.9\%$ and $v_f = 0.013$ is chosen to be approximately at the compressive strength of the pristine IMCC. Damage stages III, IV, and V are located in the softening regime of the composite at strains of 1.2%, 1.5% and 1.8% and failed ceramic fractions of 0.066, 0.134, and 0.185, respectively.

Unloading up to the initial state ($\varepsilon = 0$) of the IMCC was simulated at the five stages in order to determine the reduction of elastic stiffness due to damage of the ceramic. The unloading behavior is depicted in Figure 10 as colored lines with circle symbols. A linear stress decay is observed directly after the load change, as expected by theoretical considerations. However, approaching $\sigma = 0$, the unloading curves of all damage stages exhibit nonlinearities. They are caused by the penalty contact formulation when the rigid plates loose contact to the IMCC and due to the fact that a small amount of damage occurs in the ceramic during unloading caused by the elastic spring back of the metal phase. From the linear part of the curves, elastic moduli of 117.0, 113.2, 105.7, 99.3, and 91.9 GPa have been determined for the damaged composite at the stages I–V, respectively.

After complete unloading, a reloading up to a strain of 3% has been simulated to obtain the compressive strength $\sigma_{max}^{d,s}$ and the residual strength $\sigma_{res}^{d,s}$ of the damaged composite (superscript d) at all stages ($s = I - V$). In Figure 10, the reloading curves are plotted as colored dashed lines. The reloading behavior of the damaged composites equals the unloading behavior upon a certain point. This point varies for the different damage stages. At stage I, the reloading almost perfectly coincides with the
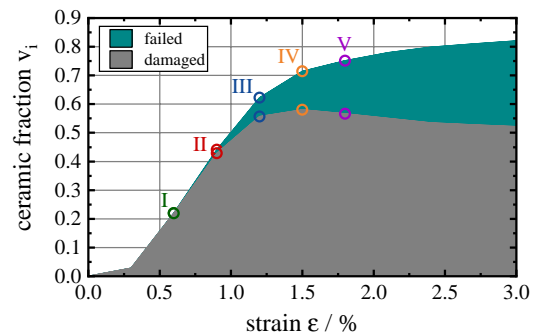

Figure 11. Fraction of ceramic exhibiting first damage (damage initiation criterion is met) and fully failed ceramic fraction (complete loss of stiffness) over the compressive strain for the first loading of the pristine composite. The colored circles mark the damage stages I–V shown in Figure 10.

**ADVANCED
SCIENCE NEWS**

www.advancedsciencenews.com

**ADVANCED
ENGINEERING
MATERIALS**

www.aem-journal.com

unloading, and only a slight nonlinear deviation of the curve is observed just before the strain prior to the unloading $\varepsilon = 0.6\%$ is reached. Subsequently, the stress–strain response is comparable to the pristine IMCC up to the compressive strength, except for the lower compressive strength of $\sigma_{max}^{d,I} = 487.7\,MPa$. For damage stage II, the deviation close to $\varepsilon = 0.9\%$ is more pronounced and the compressive stress peak $\sigma_{max}^{d,II} = 486.3\,MPa$ is shifted to higher strains, i.e., $\varepsilon = 1.13\%$ compared to the pristine composite ($\sigma_{max}^{p} = 493.8\,MPa$ at $\varepsilon = 0.99\%$). The compressive strength of the damaged material at stage II is lower compared to the pristine composite; however, it is higher than the stress at the point of unloading initiation $\sigma = 477.3\,MPa$. For the stages III–V, the initial nonlinear deviation shifts to lower stresses for increasing predamage both in terms of absolute values and in relative manner compared to the respective unloading point. The maximum compressive stresses of the reloaded structures 427.7, 387.1, and 340.6 MPa are all below the unloading point stresses 45.02, 408.7, and 390.9 MPa for the damage stages III, IV, and V, respectively. The residual strengths upon reloading 328.1, 329.4, 329.4, 325.2, and 323.9 MPa for all stages I–V coincide with $\sigma_{res}^{p} = 326.2\,MPa$ within a range of $\pm 1\%$.

As described in Section 3.2, a numerical healing routine has been applied to microstructures at all damage stages I–V in which the failed ceramic elements have been replaced with AlSi10Mg. Here, the state of failed elements at the beginning of the unloading (cf. Figure 11) is used as a basis for the numerical healing procedure. Since the real experimental healing routine includes a heating up to the melting point of the metal phase, the loading history of the aluminum alloy is ignored, i.e., residual stresses and plastic deformations are neglected. The mechanical behavior of the healed microstructures at the different predamage stages under compressive load is depicted in **Figure 12**. The healing stages I–V correspond to the respective damage stages shown in Figure 10 and 11. The key properties $E^{h,s}$, $\sigma_{max}^{h,s}$, and $\sigma_{res}^{h,s}$ for the healed (superscript h) microstructures at every healing stage ($s = I - V$) are summarized in Table 3. In general, a decrease of the elastic stiffness and the compressive strength as well as an increase of residual strength can be observed with increasing healing stage.

For stages I and II, the mechanical properties of the pristine material can be restored to a high degree with healing efficiencies of $\eta_1(E, \sigma_{max}, \sigma_{res}) > 0.99$ (see Table 3). Starting from stage III, the healed structures show a successive reduction of σ_{max}, a shift
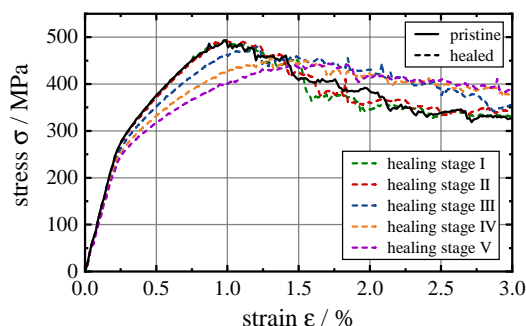
of the peak stress value to higher strains and increasing σ_{res}. Up to stage V, the healing efficiencies compared to the pristine IMMC reduce to $\eta_1(E) = 0.893$ and $\eta_1(\sigma_{max}) = 0.898$ for stiffness and compressive strength and increase to $\eta_1(\sigma_{res}) = 1.179$ for the residual strength. The healing efficiencies $\eta_1(f)$, $\eta_2(f)$ for $f = \{E, \sigma_{max}, \sigma_{res}\}$ at all and healing stages are summarized in Table 3.
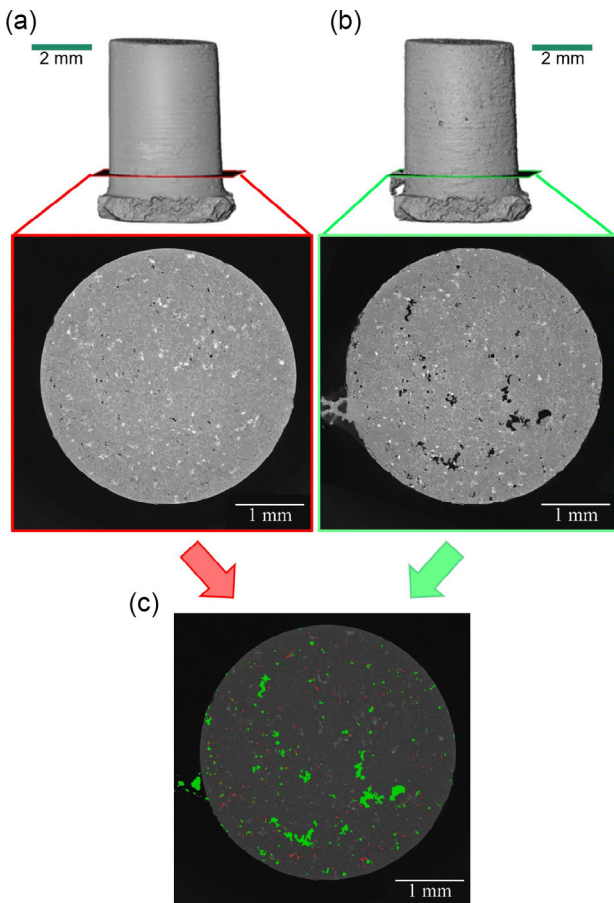
5.3. Experimental Results

5.3.1. Preliminary Test and Self-Healing Approaches

The first healing attempt, triggered by temperature only (P-A-1-650, c.f Table 2), effected an outflow of the aluminum alloy contained in the sample. This could be concluded from an alloy accumulation on the sample surface (see **Figure 13**) on the one hand and from the CT examinations on the other hand: As CT-imaging revealed, this healing approach resulted in an 2.5-fold increase of porosity compared to the unprocessed state. Furthermore, a pore-rearrangement occurred, i.e., some pores that were already present in the material before the healing attempt could no longer be found at the same location afterwards. Such a pore closure is marked with a blue arrow in Figure 13. A more detailed analysis of the pore distribution is shown in **Figure 14**. The porosity of the unprocessed sample is colored green, whereas the porosity after healing is colored red. Only slight changes could be observed regarding the crack thickness displayed in Figure 13: Some crack parts became thinner (green arrow), e.g., shows a decrease in crack width from 13.5 to 6.5 μm, whereas other cracks widened (red arrow), e.g., from
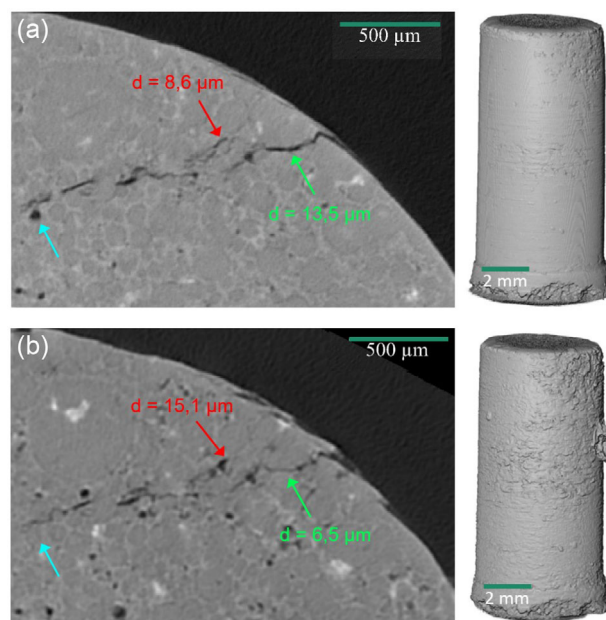
Figure 13. CT-images of a crack and the corresponding sample P-A-1-650 according to ref. [64]: a) in predamaged state and b) after self-healing. The cross-sections show in dark gray the metallic phase, in lighter gray the ceramic phase, and cracks and porosity are given in black. The blue arrows pointing on a pore disappearing after self-healing, the red and green arrows marking crack positions that became bigger/smaller due to self-healing.

Figure 12. Compressive stress strain behavior of microstructures healed at the different damage stages I–V shown in Figure 10 and 11.
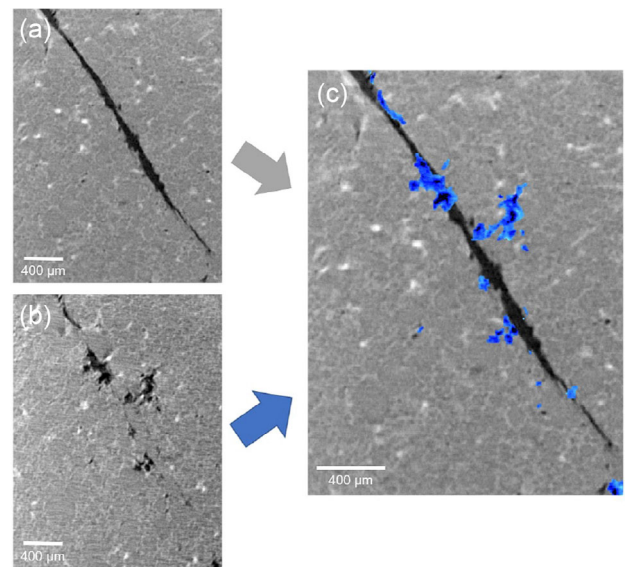
Figure 14. CT images of specimen SH-Vac-0-630 a) before and b) after self-healing. c) Illustration of porosity before (red) and after self-healing (green) indicating porosity-rearrangement.

Figure 15. Magnified CT-images of sample H-Ar-60-700 a) before and b) after the healing approach with additional alloy. Both CT-images are overlapped in c), where the porosity after healing is highlighted blue.

sample H-Ar-60-700 (c.f. Table 2). The 3D CT data evaluation method described in Section 4.4 gives insights into the decrease of crack volume (compare **Figure 15** and **16**) and the partial formation of porosity in the former crack area. The evaluation of the CT data revealed a crack volume of only 0.6 vol% for the healed sample, whereas the predamaged, unhealed sample exhibited a crack volume of 2.8 vol% (compare green highlighted area on the left side in Figure 16). Nevertheless, some parts of the crack remained unfilled after healing. Besides that, porosity could be detected in the surrounding areas of the crack as shown in

8.6 to 15.1 μm by the thermally activated healing approach. Healing success regarding Equation (2) shows values of $\eta_1(d) = 51.8\%$ and $\eta_2(d) = -75.6\%$. In general, the healing procedure has an influence on the crack morphology, as the cracks seem to have a more rounded shape after the preliminary test.

It was expected that an application of gas pressure during the temperature driven healing would prevent the alloy outflow and force the aluminum melt into the cracks. However, the samples healed with an additional gas pressure showed similar behavior as the specimen healed without gas pressure (temperature only). An outflow of aluminum alloy as well as increased porosity and only slight changes in crack thickness could be observed. Various adjustments of atmosphere, prepressure, and temperature did not improve the microstructural results. Also, the BN-coating and the plaster shell (c.f. Table 2) did not impede the alloy melt from leaving the sample. The aluminum either gathered on the top surface which was not covered by plaster or infiltrated the porous plaster shell.
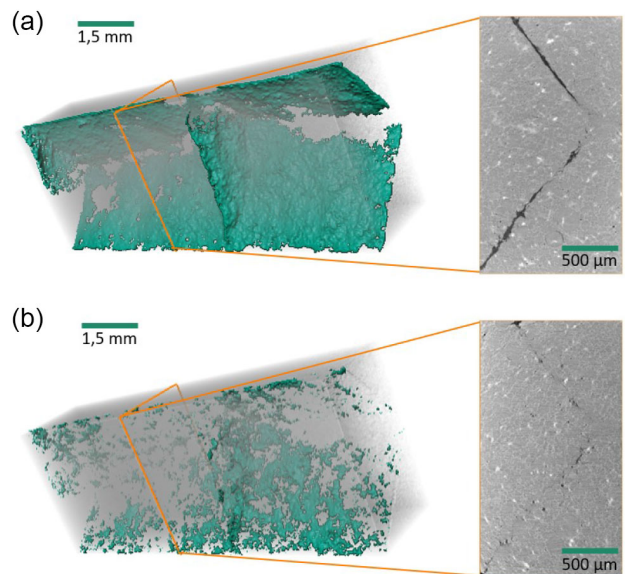
5.3.2. Healing Approach

By adding AlSi10Mg alloy prior to temperature- and pressure-assisted healing, partial crack closure could be observed in

Figure 16. Crack volumes (left) and corresponding CT-image sections (right) of sample H-Ar-60-700 a) in predamaged state and b) after healing with additional alloy according to ref. [64].

Figure 15. As this porosity cannot be found in the CT images prior to healing, a pore formation due to healing can be concluded. However, the cavities in the healed specimen have a circular shape, and sharp crack tips are no longer present in the sample. Figure 16 shows the 3D-volume of the crack before and after healing of sample H-Ar-60-700, clearly indicating a strong decrease in crack volume.

5.3.3. Soldering of the Crack

The most promising results were obtained with the flux and solder supported healing approach. **Figure 17** shows CT image sections of the corresponding sample SC-A-1-500 after healing, where the bright white regions represent the tin-based solder. The high density of tin enables a clear distinction between IMCC and solder, as tin absorbs almost all X-rays. It can clearly be detected that not only the wide shear crack was healed, but even small debonding cavities were filled by the solder. However, some hardly accessible cracks were not filled completely by the solder, leaving the crack tips open as shown in the magnified areas of Figure 17.

To analyze the influence of the healing experiments on the mechanical properties, the elastic constant in compression direction has been measured in the undamaged, damaged, and healed state after crack soldering. Four samples have been tested, and the results are shown as relative stiffness values compared to C_{22} of the respective undamaged sample in **Figure 18**. All samples show a clear decrease in stiffness due to damage, and the mean value of the stiffness loss is 12% with a standard deviation of 5.0%. As the given experiments were stopped at a certain force drop (compare Section 4.2), the amount of damage introduced to each sample cannot be adjusted exactly, and the damaged stiffness varies between 81.7% and 92.5% of the original stiffness.

An increase of the elastic constant after crack soldering is determined for three of the four samples. As the microstructural investigations showed, sample three has a very different damage structure compared to the other samples. This infuences the behavior during soldering, which can explain the lack of stiffness
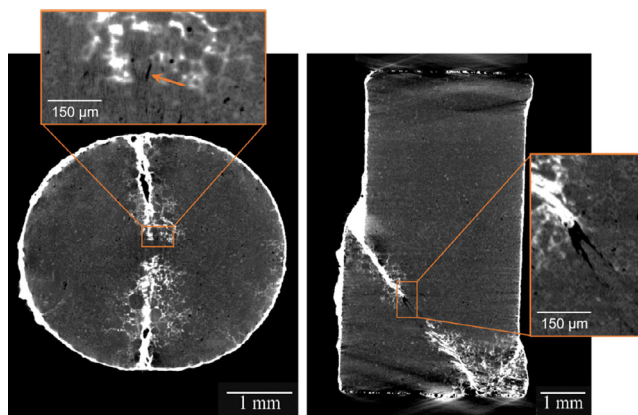

Figure 18. Relative stiffness in loading direction C_{22} for the undamaged, damaged, and solder healed composite compared to undamaged sample. Results of four different samples as well as the average value and the standard deviation are shown, respectively.

increase after solder healing. Therefore, the sample is not taken into account for the further comparison. The healed samples exhibit 85.6% up to 96.3% of the original stiffness resulting in a mean value of 91.8% with a standard deviation of 5.5% (for the adjusted evaluation. Including all four samples, a mean value of 90.0% with a standard deviation of 5.9% results, as given in Figure 18). The microstructural CT-observation shows that cracks get healed from the surface, analogous to Figure 17. Cracks in the inner part of the sample are likely to remain open as they are inaccessible for the solder entering from the outside. With the results presented in Figure 18, the mean experimental healing efficiencies for the elastic stiffness in compression can be quantified as $\eta_1(C_{22}) = 0.918$ (ranging from 0.856 up to 0.963) and $\eta_2(C_{22}) = 0.317$ (ranging from 0.214 up to 0.504).

6. Discussion

6.1. Simulation

The results of the 2D model presented in Section 5.1 showed the dependencies of stress reduction in front of a crack tip under tensile load. As expected, the stress reduction increases with increasing healing ratio A_h/A_c and crack length ratio a/w as well as with a decreasing crack opening angle α. Within the chosen parameter range, the a/w ratio shows major influence on the σ_h/σ_c ratio. This can be explained by the absolute increase of the boundary length at the bottom ($y = 0$). It increases with increasing a/w ratio, which improves the distribution of the acroscopic load $\hat{\sigma}$. Similar explanation can be used to describe the influence of the healing ratio within a range of $A_h/A_c = 0.5 - 0.9$ on the stress reduction. Compared to the a/w ratio, the influence is slightly smaller. Considering a crack of a certain length healed to a certain amount this means: for stress reduction improvement, it is more beneficial to heal a longer crack with the same healing ratio A_h/A_c than a crack of the same length to a higher A_h/A_c ratio.

However, it is different for a complete crack healing, i.e., $A_h/A_c = 1.0$. The stress concentration due to the sharp V-notch

Figure 17. Horizontal and vertical CT-image sections of sample SC-A-1-500 healed by soldering. Due to the high X-ray absorption of the solder, the sample and the cracks are given in dark grey and black. The solder is represented by the bright phase. Open crack tips, not filled by the solder, can be observed in the magnified areas framed orange.
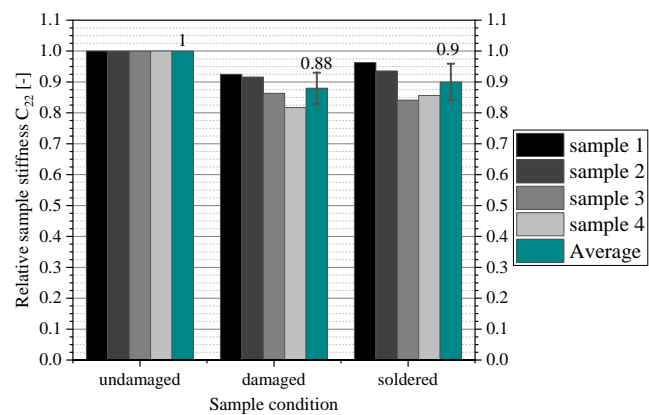
gets significantly reduced when aluminum is present directly at the tip, which is not the case for healing ratios lower than 1.0. Compared to the effects of crack length and healing ratio, the opening angle has minor influence on the σ_h/σ_c ratio, especially for high values of α. Using a geometrically sharp V-notch in the simulation model results in almost the same stress concentration in front of the crack tip independently of the opening angle, at least for the chosen α-range in this study. Therefore, the stress reduction is mainly a result of the influence of α on the bottom boundary length, analogous to the a/w ratio. Extending the α-range to larger angles would result in decreasing stress concentrations at the tip and therefore show a larger impact on the σ_h/σ_c ratio.[57] However, it should be noted that only an angle range up to 45° has been considered in this study to investigate the most probable and critical crack shapes that occur in the ceramic.

The transfer to a 3D microstructure including damage initiation and progression in the ceramic presented in Section 5.2 reveals the influence of healing on the IMCC overall mechanical properties depending on the damage stage. As assumed, the elastic modulus E and the compressive strength σ_{max} of the reloaded microstructures decrease with increasing damage stage $I–V$ due to the increasing amount of failed ceramic phase (cf. Figure 11).

For the reloading behavior of the predamaged IMCCs, two groups can be identified: 1) preloading up to the maximum compressive strength σ_{max}^p at $\varepsilon = 0.99\%$ containing stage I and II and 2) preloading beyond $\varepsilon > 0.99\%$ including stages III–V. For group (1), the initial unloading stress is lower than the respective $\sigma_{max}^{d,s}$ at reloading. Further, E and σ_{res} show only a minor reduction compared to the pristine microstructure, i.e., in the ratio between damaged and pristine elastic modulus $E^{d,s}/E^p$ at stage s is 0.976 and 0.944 for stages I and II, respectively. The corresponding maximum strength ratios $\sigma_{max}^{d,I}/\sigma_{max}^p = 0.985$ and $\sigma_{max}^{d,I}/\sigma_{max}^p = 0.967$ are very close to 1 as well. For group (2), the initial unloading stress is higher than the respective $\sigma_{max}^{d,s}$ at reloading, and the stress–strain curves do not exhibit a clear stress maximum peak. The elastic and strength ratios decrease to $E^{d,V}/E^p = 0.766$ and $\sigma_{max}^{d,V}/\sigma_{max}^p = 0.690$ at stage V. These differences can be explained by the enhanced increase of failed ceramic fraction starting after healing stage II. The reason is a change of damage mechanism in the ceramic from crack initiation before σ_{max} to crack growth and coalescence beyond σ_{max} as described in ref. [34].

In contrast, the residual strength for all damage stages coincides with σ_{res}^p of the pristine composite. Here, the volume fraction and microstructure of the aluminum alloy, which is equal for all stages, are determinants for the mechanical behavior. Small deviations between pristine and predamaged microstructures can be explained by slight variations in the damage pattern due to numerical fluctuations.

The healed composite exhibits improved mechanical properties compared to the predamaged IMCC in every damage stage. The residual strength of the healed IMCC is even higher than the pristine σ_{res}^p due to the added AlSi10Mg fraction and increases with the healing stage number (I–V). Similar to the damaged microstructures, the healing stages can be divided into two groups, 1) I & II; and 2) III–V. According to the healing efficiencies η_1 in Table 3 and the stress–strain curves in Figure 12,

microstructures at stage I and II show almost similar mechanical characteristics as the pristine IMCC, whereas stages III–V exhibit a clear reduction of E and σ_{max}. Although the absolute values are much lower, the same tendencies can be observed for $\eta_2(E)$ and $\eta_2(\sigma_{max})$. The healing efficiency $\eta_2(\sigma_{res})$ yields values that are either very high (see Table 3 stages IV and V) or negative (stages I–III) and therefore physically not meaningful. This is due to the fact that $\sigma_{res}^{d,s}$ is very close to σ_{res} for every stage s. Subsequently, the denominator in Equation (2) is either a small positive or negative number, leading to healing efficiencies without significance.

To compare the findings of the 3D microstructure and the 2D crack tip model, the ratio of compressive strength between the healed and damaged microstructure $\sigma_{max}^{h,s}/\sigma_{max}^{d,s}$ at a stage $s = I - V$ is contrasted to the stress reduction at the crack tip $\sigma_y^{h,I}/\sigma_y^c$. This ratio is minimal for stage I $\sigma_{max}^{h,I}/\sigma_{max}^{d,I} = 1.01$ and maximal at stage V where the healed microstructure can withstand macroscopic stresses that are 30% higher compared to damaged microstructure with $\sigma_{max}^{h,V}/\sigma_{max}^{d,V} = 1.30$. This is less than the stress reduction prediction in the 2D model at $A_c/A_h = 1$ in the worst case for $a/w = 0.2$ and $\alpha = 45°$ with $[\sigma_y^h/\sigma_y^c]_{a/w=0.2}^{\alpha=45°} = 0.536$. The discrepancy can be explained by numerous reasons: First, the load condition at crack tips in the 3D microstructure is different from the idealized 2D model. Second, cracks do not form only perpendicular to the ceramic rods but are triggered by maximum principal stresses which depend on the geometry of the microstructure. In contrast to the idealized 2D model, this can lead to cracks that are not aligned with the macroscopic load direction, i.e., at the ceramic aluminum interface. There can also be multiple cracks within a ceramic rod that interact with each other, which is not covered by the 2D model. Further, due to the chosen load $\hat{\sigma}$, the AlSi10Mg deforms only elastically in the 2D model. However, in the 3D model, plasticity of the aluminum becomes relevant and reduces the stress reduction in the ceramic in the vicinity of crack tips. Therefore, σ_y^h/σ_y^c and $\sigma_{max}^h/\sigma_{max}^{d,s}$ do not correlate directly. However, the range that is covered by the maximum and the minimum compressive strength ratio $\sigma_{max}^{h,V}/\sigma_{max}^{d,V} - \sigma_{max}^{h,I}/\sigma_{max}^{d,I} = 0.29$ is comparable to $[\sigma_y^h/\sigma_y^c]_{1.0}^{45°} = 0.30$. This shows that the findings of the 2D model can help to understand the behavior in the 3D composite although there are many more factors influencing the local behavior in the complex microstructure.

6.2. (Self-)Healing Experiments

While the simulation intended to show the effects of complete healing on the material properties, the experimental investigations served to determine to what extent crack healing can be realized in the interpenetrating composite. In this context, the definition of (self-)healing should be discussed, considering the applicability to IMCCs. The differentiation between autonomous and nonautonomous self-healing according to Gosh et al.[29] cannot be transferred to IMCCs because activation from an external trigger is always required for the metallic phase to perform healing. Instead, a more extensive distinction can be made. According to its definition, the term self-healing includes

the application of external energy, but not the addition of material. Keeping this in mind, the alloy-supported experiments described in Section 4.3.2 and 4.3.3 can be defined as healing experiments, whereas experiments without additional alloy (c.f. Section 4.3.1) can be defined as self-healing approaches.

Considering the results of crack healing presented in Chapter 5.3, the healing success η_2 mentioned in chapter 2.3 can be determined. For the healing approach, the crack volume evaluated from CT-imaging (see Figure 16) served as a property of interest for the calculation of the healing efficiency, labeled $\eta_2(V)$ in the following. This evaluation was not possible for the preliminary test and self-healing approaches due to the accompanying increase of porosity. Therefore, the changes in crack thickness shown in Figure 13 were used for the determination of $\eta_2(d)$ in case of the self-healing experiments. As already mentioned, the majority of cracks did not change, although some cracks parts became thinner or wider. As a result, different values for $\eta_2(d)$ could be obtained. For example, the widening of the crack marked with the red arrow in Figure 13 results in a negative healing success of $\eta_2(d) = -0.756$, whereas the crack part marked with a green arrow became thinner, showing a healing success of $\eta_2(d) = 0.518$. The reason for the increased porosity and little crack changes in the self-healed samples is the outflow of aluminum, which is caused by the poor wetting of the material system.

$$p = \frac{2\sigma_{\mathrm{L}} \cdot \cos\theta}{\frac{1}{2}d} \tag{7}$$

The capillary pressure p depends on the surface tension σ_{L}, the crack diameter d, and predominantly on the contact angle θ between alloy melt and ceramic. The wetting angle θ defines whether a liquid fills a capillary independently or not. For the nonwetting material combination of alumina and aluminum, the value of θ is greater than 90°,[58] resulting in a negative capillary pressure p according to Equation (7). The high capillary resistance makes it more beneficial for the aluminum melt to leave the specimen than entering narrow cracks. This is confirmed by the unsuccessful preliminary test, resulting in an outflow of alloy instead of self-healing.

However, in contrast to theory,[58] the capillary resistance could not be overcome by applying gas pressure up to 60 bar during the self-healing experiments. Even barriers against an alloy outflow in form of boron nitride coating and plaster embedding could not make crack penetration more favorable. The most probable reasons for these observations can be found in the physical characteristics of the aluminum alloy. First, the natural oxide layer of aluminum alloys must be considered, which not only represents a surface resistance[59] but also worsens wetting with increasing layer thickness: Experiments showed a minimization of contact angle θ down to 90° with decreasing oxide layer thickness.[60] At temperatures above 500 °C, oxide layer is 1000 times thicker form than at correspondingly lower temperatures.[59] It can be concluded that during heating up to the healing temperature of 650 °C, an oxide layer of high thickness has formed within the cracks, inhibiting wetting and self-healing. Another reason for the insufficient self-healing success can be found in the thermal expansion of aluminum. Skirl et al.[61] investigated the thermal expansion behavior of alumina-aluminum interpenetrating composites and noticed a temperature- dependent strain

hysteresis of the material. They suggested that the alloy flows back and forth in the ceramic surface channels upon cooling and heating, respectively. In combination with the oxide layer covering the crack surface, it can be assumed that it is more favorable for the aluminum melt to expand by leaving the ceramic foam rather than filling the cracks within the sample.

The healing and solder approaches served to prove these assumptions. By adding additional AlSi10Mg aluminum alloy, a counterpressure acted on the sample surface upon thermal expansion of the alloy. With the help of gas pressure, the additional alloy infiltrated the cracks, resulting in an evenly distributed healing with a healing success of $\eta_2(V) = 0.786$ regarding the crack volume V. Another benefit may be the geometry of the parallelepiped sample, making the crack more accessible for the additional alloy melt compared to the cylindrical samples. The residual porosity within the filled crack is probably the result of alloy shrinkage during cooling.

In this context, the increase in porosity after all (self-)healing attempts has to be emphasized. A comparison of the pore locations before and after (self-)healing was carried out to identify potential causes. Concerning the pore locations of the self-healed samples, no patterns or regularities can be recognized, indicating a random porosity formation and rearrangement process due to alloy outflow as shown in Figure 14. In the healed sample H-Ar-60-700, the outflow of the aluminum within the specimen could be prevented by the added alloy. Figure 15 shows that the majority of newly formed pores are located in the immediate vicinity of the cracks. It can be assumed that a movement of the specimen's aluminum into adjacent cracks occurred, resulting in open pores in the crack surrounding areas. If this was the case, one could speak of self-healing. However, it is not possible to trace the flow movement of the melt during the healing attempt, so this assumption cannot be proven.

The results of the soldering attempt shown in Figure 17 verify the existence of an oxide layer within the crack. The solder flux successfully removed the nonwetting passivation layer, enabling the solder to fill wide cracks and small cavities. Even though the solder material is much weaker than the AlSi10Mg, sharp crack tips can be sealed by this approach, reducing local stress concentrations.[25] Nevertheless, some crack tips were found to be not completely filled (c.f. Figure 17), acting as potential locations for crack propagation in case of reloading. The minimization of local stress can also be observed after the healing approach: Although the filled cracks contain some residual porosity, the resulting cavities show a circular geometry and even former crack tips have been rounded by the healing procedure. This effect can even be detected in Figure 13, however, in a less pronounced way.

6.3. Comparison of Numerical and Experimental Investigations

In this study, the numerical investigations are based on idealized model assumptions leading to possible deviations from the real material behavior. For example, a complete healing of all cracks in the 3D microstructure model and a perfectly bonded Al_2O_3/AlSi10Mg interface (in both models) have been assumed. Further, the minimum thickness of healed cracks is limited to the element size, as complete ceramic elements have been replaced with metal in the numerical healing routine. This is

a simplified assumption, which leads to different ceramic and metal volume fractions in the pristine and the healed composite. The elements in which damage initiation has started but has not proceeded to complete failure (see Figure 11, gray) are neglected in the healing algorithm, and their state of damage is lost in the healed microstructures. Due to the random volume fraction and arrangement of the pores after healing, it is very difficult to incorporate porosity in the simulations. Assumptions about pore sizes, shapes, and locations would have to be made, which all have an unknown impact on the simulation. Therefore, an ideal composite without residual porosity has been investigated numerically to reduce the amount of possible impact factors and to get insights in to the dependencies of the other parameters. All of these model assumptions lead to the best possible restoration of mechanical properties that can be achieved by (self-)healing.

Consequently, the healing efficiencies of mechanical properties in the experiments are expected to be lower than in the simulations. Using a test setup with a force drop criterion of 7% with respect to the compressive strength (c.f. Section 4.3), the UPS measurements shown in Section 5.3.3 are performed on a specimen with an amount of damage comparable to stage III of the simulations. However, the healing efficiencies of the elastic properties values $\eta_i(C_{22})$ from experiments are lower as the respective values determined numerically at stage III $\eta_i(E)$ and rather comparable to the results of higher damage stages. The range of $\eta_1(C_{22})$ from 0.856 to 0.963 covers the numerical healing efficiencies from stage III ($\eta_1(E) = 0.957$) down to stage V ($\eta_1(E) = 0.893$), and the mean value $\eta_1(C_{22}) = 0.918$ matches very well with the simulation result for stage IV ($\eta_1(E) = 0.919$). For the healing coefficient η_2, the difference becomes even more evident. The whole experimental healing efficiency range with a mean value of $\eta_2(C_{22}) = 0.317$ is lower than the numerical range, and only the coefficient for sample one $\eta_2(C_{22}) = 0.504$ is close to the values for stage IV $\eta_2(E) = 0.529$ and V $\eta_2(E) = 0.543$ determined in the simulation.

The main reasons for this discrepancy are the residual porosity and the incomplete crack filling upon solder healing in the experiments. In contrast to the perfect healing in the simulation, the solder experiment has shown a maximum crack volume healing success of $\eta_2(V_c) = 0.786$, due to the wetting issues of the ceramic interface and the Al-alloy. Similar interface problems have been reported by Lucci and coworkers[30,31] when healing an aluminum matrix with Sn60Pb40 solder encapsulated in alumina microtubes. It has to be mentioned that the lower stiffness of the S-ZnAl22 solder used in the experiments compared to the AlSi10Mg used in the simulations also has a negative effect on the elastic properties after healing. Although no experimental testing beyond the elastic range could be performed so far, the residual porosity and the incomplete crack healing will affect the other mechanical properties σ_{max} and σ_{res} as well. As shown in Section 5.1, incomplete healing of a crack of any shape and size strongly affects the stress ratio in front of the tip.

Nonetheless, the synergy of numerical and experimental investigation leads to valuable insights. Despite the challenges of the material combination for the experimental approach mentioned in Section 6.2, the range between current experimental possibilities and idealized simulative results revealed the great potential of the self-healing process worth further exploration.

For purely metallic systems, this potential has already been shown, e.g., by Leser et al.[62] who used an 60/40 In-Sn solder coating on a titanium specimen and could reduce crack growth rates to the order of 50% after temperature triggered healing and by Zheng et al.[63] who could restore the ultimate tensile strength σ_{uts} of pure nickel by electrohealing with an efficiency up to $\eta_2(\sigma_{uts}) = 0.96$. Further, the 2D model simulations can help to understand the local load-bearing capacities of the soldered crack experiments on sample SC-A-1-500 (cf. Figure 17). Experimental investigations on the stress reduction for cracks of different length and healing completeness are cumbersome, but can easily be estimated by the model with correspondingly adjusted parameters. Finally, both models can be used for the investigation on the self-healing potentials of other interpenetrating composite systems to allow for a resource efficient and target-oriented progress in the experimental methods.

7. Conclusion and Outlook

This study presented a first attempt to investigate (self-)healing approaches on interpenetrating metal ceramic composites. It has been shown that (self-)healing can be applied to IMCCs without the need of a special microstructural design adaptation.

Numerical investigations have shown the importance of crack geometry and the amount of healing on the stress reduction in the damaged composite and the restoring of mechanical properties. The results showed an upper bound estimation revealing very good healing efficiencies for the IMCC, particularly for early damage stages prior to the compressive strength.

The experimental investigations show that healing can only be implemented to a limited extent with the aluminum alloy contained in the IMCC. The successful alloy and flux supported healing experiments prove that this is mainly due to the thermal expansion mismatch of the material system as well as the passivating layer of aluminum, which is formed in oxygen environment and worsens wetting.

The key conclusions are summarized in the following: 1) Stress reduction increases with increasing healing ratio A_h/A_c and crack length ratio a/w as well as with a decreasing crack opening angle α. For the chosen parameter range, the ratios a/w and A_h/A_c show a significantly greater influence on the stress reduction than α; 2) It is beneficial to heal a longer crack with the same healing ratio A_h/A_c than a crack of the same length to a higher A_h/A_c ratio. However, full healing of a crack up to $A_h/A_c = 1$ reduces the stress significantly and can outweigh this correlation; 3) Great healing efficiencies of $\eta_1 > 89\%$ have been determined for the IMCC under compressive loading in all investigated predamage stages $I - V$; 4) For the mechanical behavior of the predamaged and the healed IMCC, two groups could be identified depending on the preloading strain and the amount of failed ceramic. Group (1), which was preloaded up to the compressive strength of the healed material is comparable to the pristine IMCC ($\eta_1 > 99\%$), whereas group (2), which was preloaded beyond σ_{max}^p exhibits a notable reduction of the mechanical properties ($\eta_1 < 97\%$); and 5) Experimental self-healing of the IMCC triggered by heat only is not feasible due to the poor wetting behavior of the material system. However, the investigated healing approaches adding

supplementary AlSi10Mg alloy or using a low-melting solder alloy (S-ZnAl22) yield promising results.

The presented simulation results indicate that the self-healing potential of interpenetrating composites is promising. For experimental realization, the tendency to surface oxidation in the metallic phase and the repulsive surface interaction between the two phases hinders self-healing in this material system. By improving the material combination within the interpenetrating composite, a realization of experimental self-healing might be achieved. This should be the focus of future research work together with the influence of interface properties and metal phase solidification/shrinkage on the properties of the healed IMCC.

Conflict of Interest

The authors declare no conflict of interest.

Data Availability Statement

The data that support the findings of this study are available in the supplementary material of this article.

[1] S. Wenlong, C. Xiaokai, W. Lu, *Energy Procedia* **2016**, *88*, 889.
[2] A. Macke, B. F. Schultz, P. Rohatgi, *Adv. Mater. Processes* **2012**, *170*, 19.
[3] N. Kota, M. S. Charan, T. Laha, S. Roy, *Ceram. Int.* **2022**, *48*, 1451.
[4] S. Roy, K. G. Schell, E. C. Bucharsky, K. A. Weidenmann, A. Wanner, M. J. Hoffmann, *Mater. Sci. Eng., A* **2019**, *743*, 339.
[5] S. Roy, J. Frohnheiser, A. Wanner, *J. Compos. Mater.* **2020**, *54*, 2001.
[6] Y. Jin, B. Zhang, Q. Liu, Z. Zhong, H. Zhang, F. Ye, Z. Zhang, *Ceram. Int.* **2021**, *47*, 2766.
[7] Y. Holovenko, L. Kollo, M. Saarna, R. Rahmani, T. Soloviova, M. Antonov, K. G. Prashanth, S. Cygan, R. Veinthal, *Int. J. Refract. Met. Hard Mater.* **2020**, *86*, 105087.
[8] L. Fu, M. Zhou, Y. Gao, B. Ma, S. Du, F. Ning, Y. Zhang, *Appl. Surf. Sci.* **2021**, *541*, 148522.
[9] P. D. Enrique, E. Marzbanrad, Y. Mahmoodkhani, A. Keshavarzkermani, H. Al Momani, E. Toyserkani, N. Y. Zhou, *J. Mater. Sci. Technol.* **2020**, *49*, 81.
[10] S. Roy, A. Nagel, K. A. Weidenmann, *Thermochim. Acta* **2020**, *684*, 178488.
[11] D. Yang, Y. Zhou, X. Yan, H. Wang, X. Zhou, *J. Adv. Ceram.* **2020**, *9*, 83.
[12] B. Mummareddy, M. Maravola, E. MacDonald, J. Walker, B. Hetzel, B. Conner, P. Cortes, *Int. J. Appl. Ceram. Technol.* **2020**, *17*, 413.
[13] S. Wang, M. W. Urban, *Nat. Rev. Mater.* **2020**, *5*, 562.
[14] C. Dry, *Compos. Struct.* **1996**, *35*, 263.
[15] S. R. White, N. R. Sottos, P. H. Geubelle, J. S. Moore, M. R. Kessler, S. R. Sriram, E. N. Brown, S. Viswanathan, *Nature* **2001**, *409*, 794.
[16] X. Chen, M. A. Dam, K. Ono, A. Mal, H. Shen, S. R. Nutt, K. Sheran, F. Wudl, *Science* **2002**, *295*, 1698.
[17] R. P. Wool, K. M. O'Connor, *J. Appl. Phys.* **1981**, *52*, 5953.
[18] E. L. Kirkby, J. D. Rule, V. J. Michaud, N. R. Sottos, S. R. White, J. A. E. Månson, *Adv. Funct. Mater.* **2008**, *18*, 2253.
[19] Y. Chen, A. M. Kushner, G. A. Williams, Z. Guan, *Nat. Chem.* **2012**, *4*, 467.
[20] S. Gupta, Q. Zhang, T. Emrick, A. C. Balazs, T. P. Russell, *Nat. Mater.* **2006**, *5*, 229.
[21] D. G. Shchukin, H. Möhwald, *Small* **2007**, *3*, 926.
[22] B. J. Blaiszik, S. L. Kramer, S. C. Olugebefola, J. S. Moore, N. R. Sottos, S. R. White, *Annu. Rev. Mater. Res.* **2010**, *40*, 179.
[23] M. D. Hager, P. Greil, C. Leyens, S. Van Der Zwaag, U. S. Schubert, *Adv. Mater.* **2010**, *22*, 5424.
[24] Y. Yang, M. W. Urban, *Chem. Soc. Rev.* **2013**, *42*, 7446.
[25] B. Grabowski, C. C. Tasan, *Self-healing Materials* (Eds: M. Hager, S. Van Der Zwaag, U. Schubert), Vol. 273, Springer, Cham **2016**, ISBN 978-3-319-32778-5, pp. 387–407.
[26] S. An, S. S. Yoon, M. W. Lee, *Polymers* **2021**, *13*, 2297.
[27] T. Shi, J. Liang, X. Li, C. Zhang, H. Yang, *Polymers* **2022**, *14*, 4509.
[28] J. B. Ferguson, B. F. Schultz, P. K. Rohatgi, *JOM* **2014**, *66*, 866.
[29] S. K. Ghosh, *Self-Healing Materials*, Wiley, Weinheim **2008**.
[30] J. Martinez Lucci, R. S. Amano, P. Rohatgi, B. Schultz, in *ASME 2008 3rd Energy Nanotechnol. Int. Conf.*, ASMEDC, Jacksonville, Florida, USA **2008**, ISBN 978-0-7918-4323-9, pp. 79–88.
[31] J. Martinez Lucci, R. S. Amano, P. Rohatgi, B. Schultz, in *Vol. 10 Heat Transf. Fluid Flows, Therm. Syst. Parts A, B, C*, Vol. 10, ASMEDC, Boston, Massachusetts, USA **2008**, ISBN 978-0-7918-4871-5, pp. 1759–1768.
[32] O. Lavrentyeva, Deutsches Patent- und Markenamt DE 10 2025 202 277 B3, **2016**.
[33] D. Horny, J. Schukraft, K. A. Weidenmann, K. Schulz, *Adv. Eng. Mater.* **2020**, *22*, 1901556.
[34] J. Schukraft, D. Horny, K. Schulz, K. A. Weidenmann, *Mater. Sci., Eng. A* **2022**, *844*, 143147.
[35] D. Horny, K. Schulz, *J. Mater. Sci.* **2022**, *57*, 8869.
[36] S. Bao, K. Tang, A. Kvithyld, M. Tangstad, T. A. Engh, *Metall. Mater. Trans. B* **2011**, *42*, 1358.
[37] M. R. Kessler, N. R. Sottos, S. R. White, *Composites, Part A* **2003**, *34*, 8743.
[38] Y. Heo, H. A. Sodano, *Compos. Sci. Technol.* **2015**, *118*, 244.
[39] V. Srivastava, M. Gupta, *J. Intell. Mater. Syst. Struct.* **2020**, *31*, 2101.
[40] G. R. Irwin, in *Fracturing of Metals*, American Society of Metals, Cleveland, OH **1948**, p. 152.
[41] G. R. Irwin, *J. Appl. Mech.* **1957**, *24*, 361.
[42] F. A. Gilabert, D. Garoz, W. Van Paepegem, *Mater. Des.* **2015**, *67*, 28.
[43] S. D. Mookhoek, H. R. Fischer, S. van der Zwaag, *Comput. Mater. Sci.* **2009**, *47*, 506.
[44] S. Ozaki, T. Osada, W. Nakao, *Int. J. Solids Struct.* **2016**, *100–101*, 307.

**ADVANCED
SCIENCE NEWS**

www.advancedsciencenews.com

**ADVANCED
ENGINEERING
MATERIALS**

www.aem-journal.com

[45] M. Nakamura, K. Takeo, T. Osada, S. Ozaki, *Technologies* **2017**, *5*, 340.

[46] S. Ozaki, M. Nakamura, T. Osada, *Sci. Technol. Adv. Mater.* **2020**, *21*, 609.

[47] C. Gao, H. Ruan, C. Yang, F. Wang, *Polym. Compos.* **2021**, *42*, 3619.

[48] J. A. Sanz-Herrera, A. Aliko-Benitez, A. M. Fadrique-Contreras, *Int. J. Solids Struct.* **2019**, *160*, 232.

[49] V. K. Mohonee, K. Lim Goh, L. Mishnaevsky, P. Pasbakhsh, *Comput. Mater. Sci.* **2021**, *192*, 110203.

[50] C. Xue, W. Li, J. Li, K. Wang, *Cem. Concr. Res.* **2019**, *122*, 1.

[51] C. Xue, W. Li, K. Wang, D. Sheng, S. P. Shah, S. P. Shah, *Smart Mater. Struct.* **2020**, *29*, 8.

[52] H. W. Swift, *J. Mech. Phys. Solids* **1952**, *1*, 1.

[53] DIN Deutsches Insitut für Normung, *Prüfung von metallischen werkstoffen - druckversuch an metallischen zellularen werkstoffen*, Beuth Verlag, Berlin, DE **2008**

[54] J. Schukraft, C. Lohr, K. A. Weidenmann, *Compos. Struct.* **2021**, *263*, 113742.

[55] M. Liu, Y. Gan, D. A. Hanaor, B. Liu, C. Chen, *Eng. Fract. Mech.* **2015**, *149*, 134.

[56] C. F. Shih, R. J. Asaro, *J. Appl. Mech.* **1988**, *55*, 299.

[57] A. Carpinteri, P. Cornetti, N. Pugno, A. Sapora, *Int. J. Solids Struct.* **2010**, *47*, 887.

[58] M. Basista, J. Jakubowska, W. Weglewski, *Adv. Eng. Mater.* **2017**, *19*, 1700484.

[59] F. Ostermann, in *Anwendungstechnologie Aluminium* (Ed: F. Ostermann), Springer Berlin Heidelberg, Berlin, Heidelberg, **2014**, ISBN 978-3-662-43806-0, pp. 217–270.

[60] J.-G. Li, *Ceram. Int.* **1994**, *20*, 391.

[61] S. Skirl, M. Hoffman, K. Bowman, S. Wiederhorn, J. Rödel, *Acta Mater.* **1998**, *46*, 2493.

[62] P. E. Leser, N. Carolina, N. Carolina, J. A. Newman, S. W. Smith, W. P. Leser, R. A. Wincheski, T. A. Wallace, E. H. Glaessgen, R. S. Piascik, *Technical Report*, NASA, Washington, DC, **2014**.

[63] X. G. Zheng, Y. N. Shi, K. Lu, *Mater. Sci. Eng., A* **2013**, *561*, 52.

[64] J. Schukraft, C. Pieper, C. Lohr, K. Weidenmann, in *Proc. 20th European Conf. Composite Materials* (Eds: A. Vassilopoulos, V. Michaud), EPFL Lausanne, Composite Construction Laboratory, Lausanne, CH **2022**.